Materials Horizons

High entropy alloying strategy for accomplishing quintuple-nanoparticles grafted carbon towards exceptional high-performance overall seawater splitting

Journal:	*Materials Horizons*
Manuscript ID	MH-COM-03-2023-000453.R1
Article Type:	Communication
Date Submitted by the Author:	23-Jun-2023
Complete List of Authors:	Raj, Gokul; Indian Institute of Science, Material Research Nandan, Ravi; Indian Institute of Science, Materials Research Centre; Japan Advanced Institute of Science and Technology School of Materials Science, School of Materials science KUMAR, KANHAI; IISC Bangalore, Gorle, Demudu; Indian Institute of Science, Materials Research M, Ambresh; Indian Institute of Science, Centre for Nano Science and Engineering Osman, Sameh; King Saud UNiversity, Chemistry Na, Jongbeom; Korea Institute of Science and Technology, Materials Architecturing Research Center; The University of Queensland, Australian Institute for Bioengineering and Nanotechnology Yamauchi, Yusuke; University of Queensland, Chemical Engineering Nanda, Karuna; Indian Institute of Science, Materials Research Centre

New Concept

One of the bottlenecks of water splitting is requiring substantially high overpotential to override the kinetic penalties caused by oxygen evolution reaction (OER). It makes the overall process less economical and highly energy-consuming. Moreover, water splitting generally requires pure water as starting material, further complicating the overall process. On the other hand, brine is widely available as a source of hydrogen, and it covers 70% of the Earth's entire surface. However, hydrogen production using brine faces a serious challenge by Cl^- competing with OH^- resulting in a complex and unfavorable situation for the overall reaction to proceed. Herein, a high entropy nanoalloy system is designed and developed for the targeted robust and corrosion resistance, ensuring the selectivity of chlorine evolution reaction (CER) over OER depending upon the experimental conditions and ambiance. To understand the science underneath, we have employed the Mott Schottky analysis (MS analysis) to unveil the rationality of fast interfacial electron transfer arising due to band position and its bending near to interface. This scientific depth can be easily extended to develop various electrocatalysts for selective oxygen or chlorine evolution power using brine water as the complementary hydrogen evolution reaction (HER) taking place at a cathode.

COMMUNICATION

High entropy alloying strategy for accomplishing quintuple-nanoparticles grafted carbon towards exceptional high-performance overall seawater splitting

Received 00th January 20xx,
Accepted 00th January 20xx

DOI: 10.1039/x0xx00000x

Gokul Raj [a,#], Ravi Nandan [a,#], Kanhai Kumar [a], Demudu Babu Gorle [a], Ambresh B Mallya [b], Sameh M. Osman [c], Jongbeom Na [d,e]*, Yusuke Yamauchi [c,d,f] and Karuna Kar Nanda [a,g,]*

High entropy alloys (HEAs), an unhackneyed class of material, have been explored in terms of their excellent mechanical properties. Seawater electrolysis marks a step contiguous to the sustainable solution to the comprehensive production of carbon-neutral fuels such as H_2, O_2, and industrially demanding Cl_2. Here in, we report for the first time a practically viable FeCoNiMnCr embraced HEA supported on conductive carbon-based seawater electrolysis along with its comprehensive hydrogen evolution reaction (HER), oxygen evolution reaction (OER), and chlorine evolution reaction (CER) kinetic studies. As an electrocatalyst, HEAs grafted on carbon black show trifunctionality with blistering kinetics, selectivity, and enduring performance towards the overall seawater splitting. We optimize high entropy alloy decorated/grafted carbon black (HEACB) catalysts concerning their synthesis temperature to scrutinize the effect of the varying magnitude of alloy formation in catalysis efficacy. Selectivity on two mutually competing reactions, CER and OER, in the electrochemical catalysis of seawater is pronounced in the catalysis to the pH of reaction media. We employ the Mott-Schottky measurements, the probing technique for the band structure analysis of the intrinsically induced metal-semiconductor junction in the HEACB catalyst, where it is found that the carrier density and flat band potential are favorable for the HEACB sample at optimized reaction conditions. HEACB sample intimates promising results towards overall seawater electrolysis with a net half-cell potential of about 1.65 V with good stability, which strongly gestures towards its broad practical applicability.

Introduction

High entropy alloys (HEAs) are a diverse class of materials embraced by five or more elements with atomic percentages usually ranging from 5 to 35 % with diverse mechanical and chemical properties.[1,2] The presence of multi-constituent metals escalates the entropy of the overall system and particularly for such a five-component system with metals in the equimolar ratio, the mixing entropy accounts to be about 1.61R, where R is the gas constant.[3–5] This exorbitant entropy of these materials accounts for their exemptional properties[6,7] The HEAs are usually procured as FCC, BCC, HCP, or a mixture of these phases but ideally with zero intermetallic phase segregation in the system.[8] These novel alloys initially garnered significant attention in the field of materials science and engineering due to their unique properties. Many of these alloys exhibit a higher strength-to-weight ratio, along with remarkable corrosion and fracture resistance.[9–13] This varied class of materials was still left unfathomable in terms of their comprehensive electrochemical interpretation for producing various energy-demanding products. Limited energy resources and arduous power requirements are the barriers faced by the human race today. According to the up-to-date statistics in 2021, the Covid-19 pandemic has seriously impacted the global energy demand.[14–17] To address this issue, constant efforts have been made to develop advanced energy generation and storage systems like fuel cells and batteries.[18] Hydrogen has been deemed as one of the high energy dense and potential future alternatives to fossil fuels. The total water splitting process powered through renewable sources like solar, wind, and hydropower can be elevated into the state of a reliable and renewable energy production pathway.[19] The overall water splitting is embraced by two important half reactions hydrogen evolution reaction (HER) and oxygen evolution reaction (OER). However, the current operating cell voltage for commercial electrolyzers (1.8 to 2.2 V) surpasses the theoretical value of 1.23 V by a huge margin, making the overall process less economical.[20] To address this issue, an exceedingly active and durable electrocatalyst is required to accelerate the active species adsorption/desorption process efficiently, thereby reducing the energy barrier of such thermodynamically uphill processes. The

---

[a] *Materials Research Centre, Indian Institute of Science, Bangalore-560012, Karnataka, India.*
[b] *Micro Nano Characterization Facility, Centre for Nano Science and Engineering. Indian Institute of Science, Bangalore-560012, India.*
[c] *Chemistry Department, College of Science, King Saud University, Riyadh 11451, Saudi Arabia.*
[d] *Australian Institute for Bioengineering and Nanotechnology (AIBN), The University of Queensland, Brisbane, QLD 4072, Australia.*
[e] *Materials Architecturing Research Center, Korea Institute of Science and Technology (KIST), 5 Hwarang-ro 14-gil, Seongbuk-gu, Seoul 02792, Republic of Korea.*
[f] *Department of Materials Process Engineering, Graduate School of Engineering, Nagoya University, Nagoya 464–8603, Japan.*
[g] *Institute of Physics (IOP), Bhubaneshwar-751005, India.*
[*] *E-mails: nanda@iisc.ac.in; jongbeom@kist.re.kr*
[#] *The authors have equally contributed to this work.*

current state of art catalysts for HER and OER are based on precious metals like Pt, RuO_2, and IrO_2 dispersed on suitable supporting matrixes.[4,9,21] However, despite their high efficiency in catalytic reactions, their vast adoption is, hampered by their scarcity, higher cost, and poor stability. The problem can be addressed by developing affordable, durable, and exceptionally active catalyst materials and tweaking possible extrinsic factors in transition metals and their alloys.

In light of the theoretical Volcano plot of HER, the catalytic activity primarily relies on the strength of the catalyst-H bond.[22] The multi-component alloys with diverse elements like Cu, Zn, Fe, Mo, etc., exhibit complex synergistic interactions inherited from numerous and diverse active sites.[23] Interestingly, metals like Ni, Co, and Fe bind with H with weak interaction, whereas Mo and W strap strongly with H.[24] But when we combine all these diverse metals into a single alloy, it is envisaged to bestow excellent catalytic output. This is often explained in terms of their inherent synergistic effect, which is often referred to by the term 'HEA cocktail effect'.[25] Another factor that favors the process is the partially filled *d*-band orbitals of these metals which can assist efficiently in completing the electron exchanges during a reaction cycle.[26] However, despite these advantages, such transition metal-based alloys exhibited serious shortcomings like poor corrosion resistance and leaching threats making them poor candidates for practical purposes in terms of their stability. Recently some unique HEAs have been developed for various applications like $Pt_{18}Ni_{26}Fe_{15}Co_{14}Cu_{27}$ for methanol oxidation through a one-pot oil phase method,[27] AlFeMnTiM (M = Cr, Co, Ni) based alloy for efficient degradation of azo dyes,[28] disordered CoCuGaNiZn, AgAuCuPdPt HEAs and AuAgPtPdCu predicted through DFT have been developed experimentally for carbon dioxide reduction catalysis with outstanding performance and higher turnover frequency.[29,30] In addition, FeCoNiCuZn oxide-based multi-metal alloy has been fabricated recently *via* a urea-based aqueous solution method for nitrobenzene electrocatalytic reduction,[31] in a similar vein, a highly efficient HER catalyst based on $Ni_{20}Fe_{20}Mo_{10}Co_{35}Cr_{15}$ has been also reported recently with excellent corrosion resistance in both acidic and basic reactions.[32] These findings indicate the high prospect and potential of such alloy systems in evolving into exemplary catalysts with high benchmarking according to the catalyst Figure of merit.

Along with the typical water electrolysis, seawater electrolysis also procured significant demand by the vast availability of the brine and the resulting practical products.[6,33] Since 70% of the Earth's entire surface is covered with brine, seawater electrolysis can be a very attractive and reliable gas supply system of hydrogen, oxygen, and chlorine if appropriate catalysts can be developed to selectively generate essential and expensive gases by controlling the reaction kinetics with related parameters. Generally, in the electrolysis of brine solution, the water molecules compete with the Cl^- ions at the anode side to release chlorine gas through the chlorine evolution reaction (CER), which remains an important hurdle in this method.[32,34] As a counter-reaction to the anodic potential, it is beneficial to get hydrogen gas *via* HER as the cathode product. If it can be handled by the selective oxidation of chloride ions and oxide ions along with other competing species like bromide and sulfates in the seawater, this process can be of enormous economic demand.[35] Thermodynamically the OER is preferred over the CER reaction since the standard potential for OER and CER are 1.23 V and 1.36 V, respectively.[34] But the two-electron kinetics of CER seems less sluggish compared to the four-electron kinetics of OER, which makes the chloride oxidation process favorable with slightly lesser overpotential. Therefore, one must use these basic distinctions to tweak the reaction with an efficient catalyst to get the desired product in an economically feasible pathway.

Multi-elemental HEAs have emerged as a type of catalyst material with promising physiochemical properties, capable of managing multiple reactions simultaneously because of its numerous encrypted active sites.[36] Moreover, the catalytic behavior of HEA can be enhanced by coupling them with suitable substrates such as conductive carbon, doped graphite materials, and MXenes[37,38]. Herein we report a single-step pyrolysis technique to develop a high entropy alloy of Cr, Mn, Fe, Co, and Ni on a conductive carbon black (HEACB) for the effective catalysis of HER, OER, and CER reactions by utilizing the synergistic effects of mixed metal (cocktail effect) high entropy alloys. This work involves an in-depth analysis of kinetics, impedance spectroscopy, and Mott-Schottky analysis for each reaction. This work has the potential to open new avenues for the development of a near-ideal catalyst that satisfies all the criteria outlined in the catalyst Figure of Merit. By tweaking and optimizing their inherent structural and chemical characteristics, we can aim for efficient seawater splitting. Additionally, this research aims to gain a deeper understanding of the reaction kinetics and any limitations associated with them.

Results and discussion

Characterizations of the composite alloy materials

Fig. 1a shows the X-ray diffraction (XRD) patterns of the samples prepared under different annealing temperatures. After annealing at 500 °C, the diffraction peaks corresponding to the BCC phase appear broad. As the annealing temperature increases to 750 °C, besides the diffraction peaks of the BCC-structured solid solution, diffraction peaks corresponding to the FCC and HCP phases emerge. This indicates that the alloy has a multi-phase structure with mixed BCC, FCC, and HCP phases. In addition, we observe a superlattice reflection peak (indicated by *) at ~30.24°, corresponding to the ordered B2 phase. This indicates that the alloy either has a single B2-ordered solution structure or a disordered BCC+B2 mixed phase structure. Further, the intensity of the BCC, HCP, and B2 phases decreases and completely disappears with increasing the annealing temperature from 750 to 1000 °C. Meanwhile, the intensity of the diffraction peaks of the FCC phase increases with

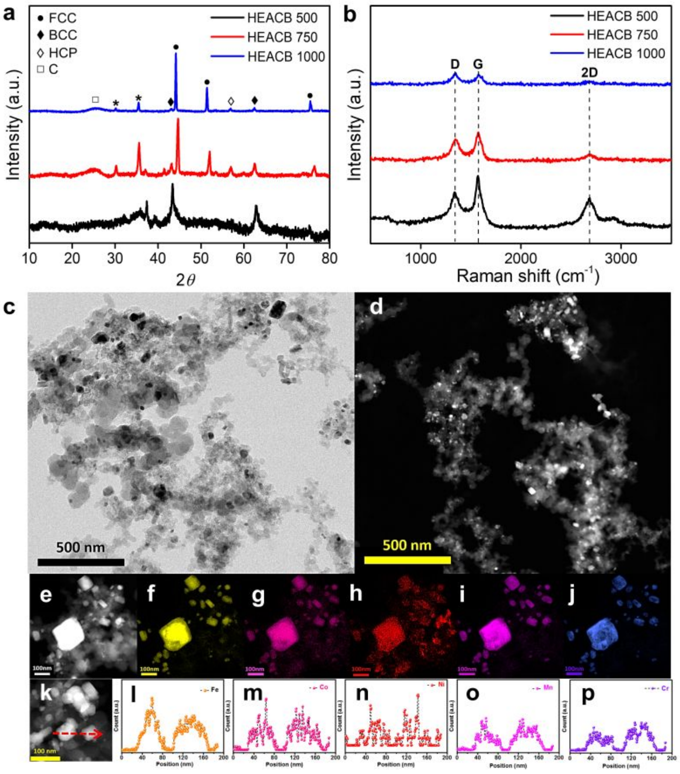

Fig. 1. (a) XRD patterns and (b) Raman spectra of HEACB samples at different synthesis temperatures. (c) HEACB 1000 bright filed TEM image, (d-e) HAADF-STEM images, (f-j) elemental maps of elements (f) Fe, (g) Co, (h) Ni, (i) Mn, (j) Cr, and (k-p) the line scan maps with the corresponding intensity profiles of individual elements.

temperature, which indicates the complete formation of a solid alloy structure in the FCC phase. We observe an additional peak at ~35.56° (indicated by *) with a dramatic decrease in intensity after annealing, probably due to impurities in the structure. In addition, we observe a broad XRD peak of ~25.18° at different annealing temperatures, confirming the presence of carbon black in the composites.

The presence of carbon in the material is confirmed by Raman spectroscopy, as shown in **Fig. 1b.** The typical Raman peaks observed at 1340 (D band), 1569 (G band), and 2685 cm^{-1} (2D band) correspond to sp^3 defects and in-plane vibrations of sp^2 hybridized carbon atoms.[39] The 2D peak suggests the C-C bond concerning sp^2 domains in the material without much strain in between the bonds. The I_D/I_G ratio provides information on structural defects, and the defect densities (I_D/I_G ratio, **Table S1**) of the composite alloy are 0.65, 0.76, and 1.10, respectively.[40] The defect densities increase with higher annealing temperatures, which can be attributed to the resulting distortions. Furthermore, the presence of defects reduces the intensity of I_{2D}/I_D, and this value decreases as the annealing temperature increases due to the declining crystallinity of sp^2 domains.

To obtain a direct visualization of the samples at different annealing temperatures, we employed scanning electron microscopy (SEM) analysis (**Fig. S1**). There is no discernible effect on the morphology of the particles at temperatures of 750 and 1000 °C. **Fig. S1e-k** shows the elemental mapping from energy-dispersive X-ray spectroscopy (EDS) analysis within a selected area (HEACB 1000). This emphasizes the homogeneous distribution of all the elements throughout the structure, hence confirming the successful alloy formation. The percentages of constituent elements in the alloy were determined by EDS spectrum analysis, with the data provided in **Table S2**. The alloy exhibits an almost uniform distribution of constituent elements, indicating the formation of HEAs. However, the alloy contains a higher amount of carbon compared to other elements, suggesting the presence of carbon black as the primary catalyst substructure in the material.

To obtain more detailed and highly resolved images of our sample, we employed Transmission Electron Microscopy (TEM). The bright field TEM image in **Fig. 1c** and the high-angle annular dark field (HAADF) scanning mode image in **Fig. 1d** show the HEA nanoparticles embedded in the carbon black matrix. A representative particle in the HAADF-scanning transmission electron microscopy (STEM) mode was scanned at high resolution, as shown in **Fig. 1e**. This image was then subjected to elemental mapping (**Fig. 1f-j**) to visualize the distribution of elements. The elemental mapping reveals a uniform distribution of all five elements in the nanoparticles, thereby confirming the formation of a homogeneous solid solution in the HEAs. The line scan (**Fig. 1k**) conducted over two randomly selected nanoparticles (**Fig. 1l-p**) also yields similar results, confirming the successful stabilization of HEA particles on a highly conductive carbon black support.

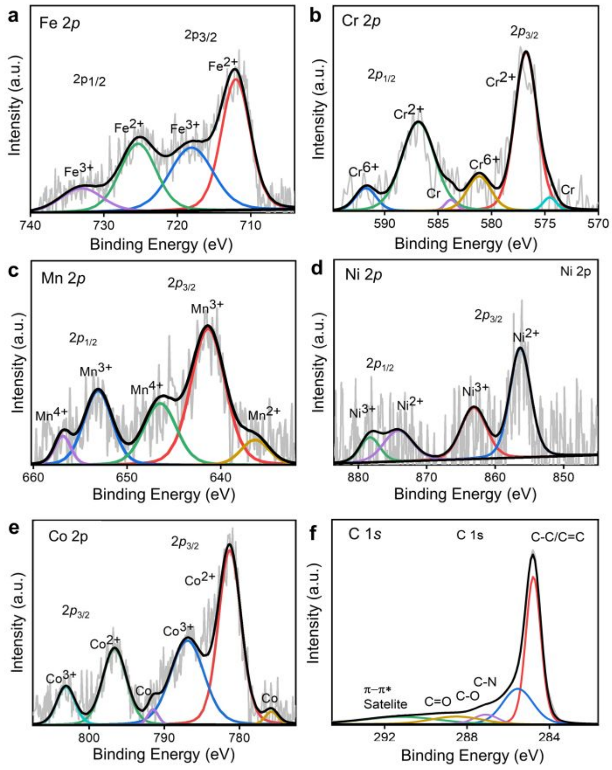

Fig. 2. XPS spectra of (a) Fe 2p, (b) Cr 2p, (c) Mn 2p, and (d) Ni 2p (e) Co 2p and (f) C 1s of HEACB 1000 catalyst.

To further shed some light on the elemental details in HEACBs, we have performed X-ray photoelectron spectroscopy (XPS) studies (**Figs. 2** and **S2-S5**). The C 1*s* peak is maintained at 284.78 eV by applying charge correction for all the samples. The deconvoluted HRXPS spectra of Fe, Cr, Mn, Ni, and Co (**Fig. 2a-e**) indicate the existence of multiple oxidation states, revealing the inherent complex electronic nature of HEAs.[25] Such a multielement alloy nature at the atomic level in HEAs is beneficial for offering near-continuous adsorption energies and can be advantageous for tuning the overall physicochemical properties of electrocatalysts for various catalytic activities.[25]

The deconvoluted C 1*s* high-resolution XPS (HRXPS) spectrum in **Fig. 2f** suggests the presence of carbon moieties such as C−C (284.78 eV), C− N (285.53 eV), C−O (287.09 eV), and C=O (288.5 eV) [25] (**Table S3**). Incorporating the metal core into the carbon matrix allows for the adjustment of adsorption energies for different electroactive species.[41] We also found that on rising reaction temperature from 500 to 1000 °C, the overall metal concentration raised and reached a maximum at 750 °C and then came down to a lesser concentration at 1000 °C, as shown in **Fig. S2**. This change in metal concentration is due to the loss of segregated phases of all elements due to evaporation at higher temperatures, which favors the alloy formation.[31] By analyzing the wide spectra of all three samples, we can see distinct oxide peaks, representing the oxidation of the sample during handling and material synthesis (**Fig. S5**). Correlating with the results from the C 1*s* HRXPS, we can ascertain that these oxygen peaks indicate the surface oxygen groups like aldehyde (-CHO) and carboxylic acid (-COOH)**.**[42] To get insight into the presence and involvement of such surface oxygen, we analyze the convoluted XPS spectrum of oxygen in detail in **Tables S4-S5** and **Fig. S5**. As the literature suggests, various oxygen present in different locations in a sample as oxygen atoms in the lattice (O_L) (~530 eV),[31] oxygen atoms in the vicinity of an oxygen vacancy (O_v) at ~531 eV [31], oxygen atoms on the outer face of the lattice structure (O_s) with a lower coordination number having binding energy nearly ~532 eV [31] and oxygen species adsorbed (O_{ads}) is located at ~533 eV [31] which may be due to the adsorption of water from the environment. Interestingly, we observe as the temperature increases from 500 °C to 1000 °C, there is an intensification of O_s peaks. Among these, O_s peaks always occupy the major contribution which once again signifies the adsorbed oxygen and surface functionalization. At higher temperatures, we find that the concentration of surface oxygen decreases, indicating improved order of crystalline in the alloy material. This aligns with accelerated alloy formation and supports the notion that higher temperatures facilitate the creation of high entropy alloys. Consequently, the HEACB 1000 system is anticipated to possess a greater abundance of active alloy sites, leading to enhanced catalytic activity, as confirmed by our electrocatalytic investigations. It is evident from numerous reports that such oxygen is beneficial in inducing defects in the system and enhancing the overall catalytic activity by favoring the preferred reaction sites for specific intermediates.[31]

Oxygen evolution reaction

Electrochemical water splitting reaction is deemed as one of the reliable and renewable means of hydrogen and oxygen production with zero carbon emission to the environment.[43] Water splitting reaction is essential in numerous technological applications like fuel cells, metal-air batteries, chemical industries, etc. Statistics show that in contradiction to the manifold advantages of electrochemical synthesis, only around 4% of the world's hydrogen demand was able to satisfy by water electrolysis.[44] One of the major hindrances in their practical application is the sluggish kinetics of the four-electron-based oxygen evolution reaction (OER). The overall reaction thus runs at a high voltage of 1.8 to 2.0 V, which demands huge electrical input and makes the overall process less feasible. To overcome this hurdle, we require an efficient catalyst to catalyze both the half-cell reactions, i.e., hydrogen evolution reaction (HER) and OER reactions together, which will significantly reduce the production cost of these gases. Among these two half-cell reactions, OER stands out to be more challenging.[45,46]

Herein, we investigate the electrochemical performance of our as-synthesized high entropy alloy samples viz HEACB 1000, HEACB 750, and HEACB 500, which were synthesized at different annealing temperatures towards OER in a 1 M KOH medium using a standard three-electrode configured CHI 750E electrochemical workstation. Linear sweep voltammetry (LSV) profiles on a glassy carbon electrode (GCE) were taken for all the samples in the OER polarization window. **Fig. 3a** shows the LSV curves of HEACB 1000, 750, and 500 samples compared to the current state-of-the-art catalyst RuO_2. As illustrated in **Figs. 3a** and **S6a**, HEACB 1000 can push current at a rate of 10 mA/cm^2 with a lesser onset and an overpotential of 350 mV, then followed by HEACB 750 (352 mV) and finally HEACB 500 (389 mV). These values reveal the superiority of the HEACB 1000 over others in efficiently operating OER kinetics.

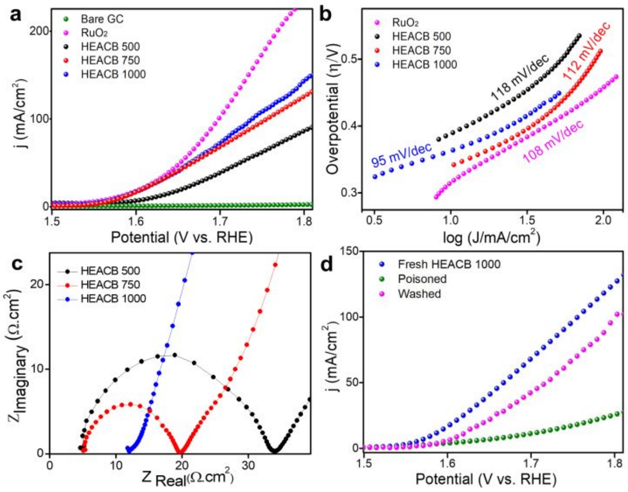

Fig. 3. (a) LSV curves of commercial RuO_2 and HEACB samples in OER polarization region in 1M KOH. (b) Tafel slopes analysis extracted from kinetic region of LSV curves (c) electrochemical impedance spectroscopic analysis of HEACB samples in 1M KOH, and (d) LSVs of the fresh, poisoned, and washed HEACB 1000 in the OER polarization region.

Even though the overpotential was slightly higher than the commercial RuO_2, in terms of reaction kinetics and overall reaction stability, HEACB 1000 is competent enough with RuO_2. The Tafel slope of a catalyst can often be correlated directly to the reaction mechanism and kinetics. A lower Tafel value indicates less energy-demanding reaction pathway and more active site exposure hence faster kinetics. **Fig. 3b** shows that HEACB 1000 possesses a comparatively lesser Tafel slope of 95 mV/ dec, concerning HEACB 750 (112 mV/dec) and HEACB 500 (118 mV/dec), which is better compared to the commercial RuO_2 catalyst (108 mV/dec) and various recently reported OER catalysts (**SI**).

Electrochemical impedance spectroscopy (EIS) probing is done to get a perception of the charge transfer resistance at the electrode/electrolyte interface in a 1 M KOH, representing the ease with which the electron transfer can happen at the heterojunction about the catalyst's intrinsic conductivity. The Tafel slopes are often expected to have direct implications with charge transfer resistance measured through EIS. **Fig. 3c** illustrates the EIS plot of as-synthesized samples, manifesting the Rct + Rs values (sum of charge transfer and solution resistance) of HEACB 1000 as 12.3 Ω, HEACB 750 as 19.7 Ω, and HEACB 500 as 33.8 Ω. Usually, an EIS spectrum with a smaller circular diameter represents a swift and augmented charge transfer capability.[38] This represents our sample HEACB 1000 upfront in terms of the charge transfer conductivity. The charge conduction between the electrolyte and multi-alloy interface appears to be more feasible due to the influence of highly conductive carbon on which the high entropy alloy has been dispersed.

The electrochemically active surface area (ECSA) represents the degree of active sites on our catalytic bed, and it can be probed in terms of the double layer capacity (C_{dl}) of a sample. The cyclic voltammetry response of HEACB 1000, 750, and 500 in 1 M KOH in the non-faradaic region and the corresponding C_{dl} value derived from the charging current vs. scan rate plot are shown in **Figs. S6 and S7**. We perceive C_{dl} values to be in the order of HEACB 1000 (11.3 mF/cm^2) > HEACB 500 (10.2 mF/cm^{-2}) > HEACB 750 (5.4 mF/cm^2). It is worth noting that HEACB 500, even though having a higher area than HEACB 750, in terms of, activity, the latter sample predominates, and this can be ascribed to the better intrinsic activity of HEACB 750 due to the better alloy formation compared to the less temperature annealed sample HEACB 500. Since ECSA has a direct correlation to the C_{dl} values, HEACB 1000 stands out to be the one with the highest ECSA.[44]

The direct involvement of the mixed metal cocktail effect of the high entropy alloy and their related active sites on the catalytic activity can evaluate by exercising a poisoning test using cyanide ligands.[47] Being a strong π acceptor, CN^- can bind with the metal centers strapped strongly and will block the approaching electroactive species, thus reducing the catalytic efficiency. **Fig. 3d** intimates the LSV curves of the poisoning experiment, where we can observe that after poisoning the catalyst with 0.1 M NaCN solution, the activity of the sample came drastically down near the bare minimum. This observation reinforces our assumption that the alloy metal centers are the nerve centers behind the promising OER performance. When the poisoned catalyst is washed with DI water to free the metal centers from the ligand hindrance, the activity regeneration can be seen near the fresh sample. The failure in complete recovery of the activity after poisoning is expected to be the combination of the incapability of the complete removal of the cyanide moieties from the already poisoned sample with mere external washing and the sample loss incurred during this cleaning process.

For an industrial catalyst to be truly effective, it must show high levels of activity and durability, even when subjected to continuous catalytic processes. So, the best-performing HEACB 1000 catalyst was tested for six hours in 1 M KOH using chronoamperometry analysis, as shown in **Fig. S6d**, to study its stability in the OER polarization region. The current-time response indicated more than ~75% activity retention post long-term chronoamperometric operation in the harsh electrolytic medium. The activity reduction we observe can likely be attributed to the harsh and corrosive conditions utilized during the OER process. Additionally, we suspect that some sample loss may have occurred on the electrode surface because of prolonged oxygen gas evolution. However, as seen in **Fig. S6d**, after the initial decline in the activity, the catalyst reaches a stable state of action where the stability seems to be retained for a longer time. This observation is quite promising for its practical usage for the OER application.

Hydrogen evolution reaction

Electrochemical hydrogen evolution reaction (HER), one of the half-reactions in total water electrolysis, is economically promising and a greener way to deliver hydrogen fuel for the ever-snowballing energy demands of humanity. This carbon-free high-energy dense fuel is a major requirement in fuel cells, automobiles, spaceships, etc. We analyze the HER performance of our catalyst on a similar 3 electrodes configured setup in 0.5 M H_2SO_4 electrolytic media. For activity comparison and

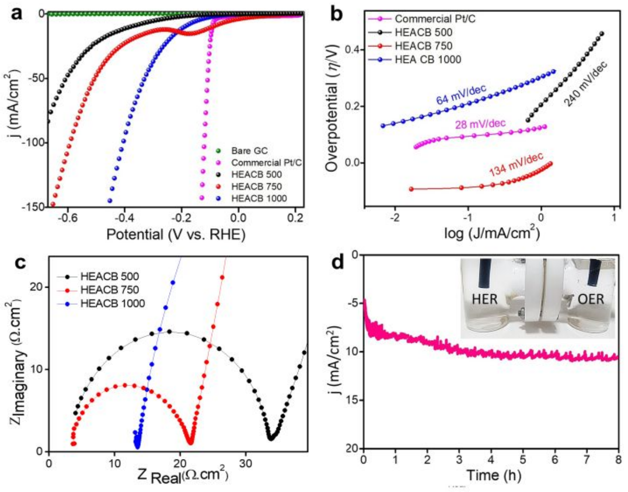

Fig. 4. (a) LSV curves of HEACB samples and commercial Pt-C in HER polarization region in 0.5M H_2SO_4, (b) Tafel plots for the respective polarization curves and (c) electrochemical impedance spectroscopic analysis of HEACB samples in 1M H_2SO_4, and (d) chronoamperometric test for HEACB 1000 in 0.5 M H_2SO_4 at room temperature in the HER polarization potential (inset: H cell in which water electrolysis is carried out).

benchmarking, commercial Pt/C has been employed. **Fig. 4a** shows the LSV at a 10 mV/sec scanning rate of all the prepared alloy samples. **Fig. S8a** shows the onset and overpotential comparison of the HEACB sample synthesized at different pyrolysis temperatures.

It is evident from the comparison plot that the HEACB 1000 with a high degree of single-faced high entropy alloys shows excellent results. In terms of these parameters related to the reaction potential, HEACB 1000 demands a lesser onset potential of 72 mV and an overpotential of 190 mV to drive a current of 10 mA/cm^2 in the HER polarization region. HER occurs by following two reaction pathways, Volmer-Tafel and Volmer-Heyrovsky pathways.[24]

Volmer – Heyrovsky pathway:
$H_2O + e^- \rightarrow H_{ads} + OH^-$ (Volmer)
$H_{ads} + H_2O + e^- \rightarrow H_2 + OH^-$ (Heyrovsky)
Volmer – Tafel pathway:
$H_2O + e^- \rightarrow H_{ads} + OH^-$ (Volmer)
$H_{ads} + H_{ads} \rightarrow H_2$ (Tafel)

Scrutinizing the Tafel slope in HER gives a lot of insights into the reaction mechanism and nature of reaction kinetics compared to OER, where later the reaction mechanism seems to be much more complex than HER.[46,48] **Fig. 4b** shows the Tafel plots for the samples along with the commercial Pt/C catalyst. Among the HEACB catalysts, HEACB 1000 exhibits the most favorable performance, as evidenced by its Tafel slope of 64 mV/dec. Tafel slope, along with the turnover frequency, exchange current density, and faradaic efficiency values (see **Tables S6-S8**), indicates that HEACB 1000, with a comparatively better and high degree of alloy formation, is capable of promoting the HER catalysis efficiently with stability, at the same time cheaper in production cost as compared with that of precious metal-based catalysts. The value of the Tafel slope 64 mV/dec propounds that the rate-determining step is the Heyrovsky step (product desorption step) for HEACB 1000, which follows a Vomer-Heyrovsky mechanism and hence has faster kinetics. Whereas in the case of HEACB 750 and HEACB 500, we witness higher Tafel values suggesting that the rate-determining step is shifted to the Volmer step, i.e., the active species adsorption step, which makes their catalysis less energy efficient and thermodynamically uphill.

To correlate and corroborate the above kinetics and activity trend, we subject the samples to EIS measurements to study the nature and charge transfer resistance of the catalyst at the heterojunction in an acidic environment. **Fig. 4c** illustrates the EIS plot for all the HEACB samples. We could infer a similar trend as we observe in basic media in the charge transfer resistance of all three catalysts, which again strengthens our observation of the trend in reaction kinetics of our samples towards HER. The electrochemical active surface area (ECSA) also plays a prominent role in defining the overall activity of the catalyst because they are a measure of the available and accessible active sites on the catalyst surface. **Fig. S8b** and **c** show the cyclic voltammetric response and the respective double-layer capacitance measurement plot in a region away from reaction species polarization. As we expect, HEACB 1000 is found to be incorporated with a more active surface area (C_{dl} =15.4 mF/cm^2) concerning the other two samples (HEACB 750, C_{dl} = 5.4 mF/cm^2 and HEACB 500, C_{dl} = 8.6 mF/cm^2). But in the case of HEACB 750, we find the ECSA is lesser than the least performed HEACB 500. This proves the less inherent activity of HEACB 500 samples despite the favorable surface area factor. The comparatively higher alloy NPs present in the HEACB 750 than in HEACB 500 and its intrinsic activity might have helped to override the surface area factor and brought up as a more efficient HER catalyst than HEACB 500.

The direct contribution of the highly active alloy metal centers to the excellent HER activity has been proven through a poisoning test. The poisoning agent used in this test was a 0.1 M cyanide ion solution, similar to the OER activity check. **Fig. S8d** shows the core observation made in the poisoning experiment. After poisoning, there was a drastic reduction in the performance, indicating the complete or partial blockage of the active metal centers, thus hindering the catalysis. The regaining of the activity after sterling the electrode surface from CN^- ions underline that the activity of our as-synthesized catalyst is solely because of the presence of the active high entropy alloy nanoparticles on the conductive carbon bed. The long-term stability of a catalyst is always of great concern when we especially look forward to a practical implication of the catalyst materials, such as in the case of practical bulk water electrolyzers. **Fig. 4d** shows the stability response curve of the best-performed HEACB 1000 catalyst in 0.5 M H_2SO_4 solution in the HER polarization region. It is evident from the current response that the sample is showing very promising stability in the HER potential range, where we can see that even after continuous operation for almost 8 hours there is no considerable degradation happening to the HER performance. Moreover, the catalyst activity is enhanced during the stability run, possibly due to the activation of metal species on the catalytic surface and the suitable charge transfer environment. Furthermore, this enhancement developed can be attributed to the constant contact with the electrolyte environment, thus retaining a stable heterojunction at the reaction interface

Chlorine evolution reaction

Chlorine is one of the industrially demanding elements, which is an important requirement for the synthesis of many chemical products like plastics, disinfectants, bleaching powders, pesticides various inorganic salts, and as well as in electronic industries.[5,34] The current chlorine requirements are satisfied by chloroalkyl electrolysis, which demands enormous investment and seriously threatens environmental health by emitting pollutants during the process. To overcome these shortcomings and fulfill the chemical demand, an ideal electrochemical oxidation process backed up by a robust and efficient catalyst is needed. A novel strategy in the same vein is to utilize the vastly available seawater as the electrolyte in the water-splitting reaction. This process appears to be a very interesting and reliable source of hydrogen, oxygen, and chlorine production if the reaction can be selectively steered toward our targeted products. Under normal conditions, in the electrolysis of seawater, water molecules compete with Cl^- ions at the anode side to release chlorine and as a counter-reaction, we will be able to extract hydrogen gas from the cathode end which makes the overall process economical and promising in terms of the production of two industrially demanding gases.[35] If we can manage the targeted oxidation of chloride and oxide ions, while also dealing with other substances like bromide and sulfates present in seawater, this process could have a substantial effect on the energy and production industries.[9,34] Herein, we are trying to explore the chlorine evolution reaction kinetics on the catalytic surface of our novel high entropy alloy embedded conductive carbon-based samples. The goal is to enhance the electrolytic process by promoting selectivity between chloride and oxide ions, resulting in non-parasitic CER and OER reactions. **Fig. 5a** shows the LSV response of the HEACB samples in a 1M HCl and 4 M NaCl medium at a scan rate of 10 mV/sec on a 3-electrode configuration-based electrochemical workstation. Thermodynamically the OER is preferred over the CER reaction. However, the two-electron kinetics of CER compared to the four-electron sluggish kinetics of OER makes the chloride oxidation process favorable with slightly lesser overpotential. **Fig. 5a** and **b** compare the relative activity of HEACB 1000, HEACB 750, and HEACB 500 with different degrees of high entropy alloy contents towards CER activity. The HEACB 1000 shows the least onset potential with an overpotential of only 30 mV to deliver a current of 10 mA/cm^2, whereas HEACB 750 and HEACB 500 exhibits overpotentials of 79 mV and 163 mV, respectively.

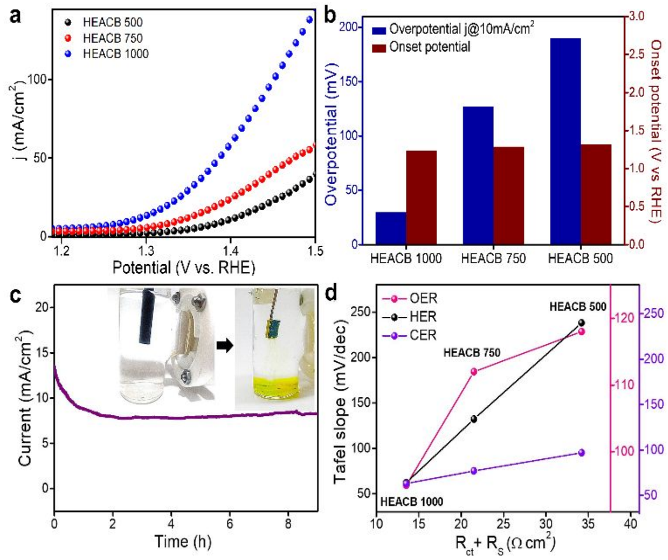

Fig. 5. (a) LSV curves of HEACB samples in CER polarization region in 0.5M H_2SO_4 and 4M NaCl. (b) comparison plot of onset and overpotential of HEACB samples. (c) Chronoamperometry test for HEACB 1000 at room temperature in the CER polarization potential, and (d) plot correlating Tafel slope comparison of HEACB samples with system resistance derived from electrochemical impedance spectroscopic analysis

The kinetics of CER is well studied on RuO_2 surfaces, and their reaction mechanism is explored. The reaction on such catalyst proceeds *via* the Volmer-Heyrovsky pathway with the desorption step being the rate-determining step,

$2Cl^- \rightarrow Cl_{ad} + e^- + Cl^-$ (Volmer step)
$Cl_{ad} + Cl^- \rightarrow Cl_2 + e^-$ (Heyrovsky step)

The Tafel slope value indicates the mechanism followed and the rate-determining step. **Fig. S9a** shows the Tafel plot analysis of HEACB samples, and it directly reflects the kinetics trend of CER reaction on the respective catalyst surfaces as HEACB 1000 (63 mV/dec) > HEACB 750 (77 mV/dec) > HEACB 500 (97 mV/dec). The lesser charge transfer resistance, higher ECSA, and BET surface area of the HEACB 1000 also seem to be intrinsically favoring factors for the observed faster catalyst kinetics.

To show the involvement of metal core centers in the catalysis, we have staged a poison test with cyanide ions, as shown in **Fig. S9b**. The contrast in the behavior before and after poisoning substantiates the active metal centers in the catalyst responsible for CER activity. To promote any catalyst towards possible practical seawater splitting application of chloride electrolysis, it is required to analyze how suitable the catalyst is in terms of its stability, especially in a corrosive and harsh seawater environment. Chronoamperometric stability analysis was carried out where the HEACB 1000 samples were run in the CER polarisation region in 4 M NaCl and 1 M HCl media for a continuous operation of about 8 h, as shown in **Fig. 5c**. The stability response shows that the HEACB 1000 retained the activity without much degradation, even in a deteriorating and hostile reaction media.

To understand the deteriorative effects on the catalyst material, a detailed chemical and structural characterization of our best-performing sample HEACB 1000 after a continuous operation of 15 hours was performed. By conducting this study, we aim to determine if our catalyst can endure the severe reaction conditions of seawater splitting and if it is a viable option for use as an electrocatalyst in practical applications. **Figs. S10-S12** and **Table S9** in the supplementary information show the detailed chemical and structural characterization of the HEACB 1000 after continuous HER, CER, and OER reactions in a seawater-simulated electrolyte media for about 15 hours of continuous operation. The improved durability of the catalyst can be attributed to the intimate contact between the dispersed HEA nanoparticles and the conductive carbon matrix. During the pyrolysis process, the conductive carbon develops a strong bond with the nanoparticles, preventing their leaching or detachment from the catalytic framework in the harsh electrolytic environment.

This intimate contact can ensure the stability and longevity of the catalyst during prolonged operation. Thus, the trifunctional HEACB 1000 seems to be a suitable and promising catalyst for the practical adoption of seawater electrolysis. The EIS results directly affect the kinetic parameter since they decide the charge transfer efficiency.[31,49,50]

To verify this, a plot was made between charge transfer resistance and Tafel slope as the kinetic parameter, as shown in **Fig. 5d**. We could see a head-on correspondence between these intrinsic factors with HEACB 1000 spotted at the most favorable place in the Tafel-R_{ct} plot, reinforcing the experimental findings we discerned in the case of HER, CER, and OER. For the HEACB 1000, we could witness that the Tafel slope and system resistance is the lowest in the case of HER, OER, and CER, gesturing its better efficiency towards catalysis. We also subjected the catalysts to BET surface area measurements, as shown in **Fig. S13,** and found that the surface area of the samples followed a similar trend as in the case of C_{dl} HEACB 1000 (84 m^2/g)> HEACB 500 (76 m^2/g)> HEACB 750 (64 m^2/g), which once again verified our inference from electrochemistry. BET surface area analysis also matches exactly with the trend in ECSA values we extracted using double-layer capacitance hence strengthening the view that the extrinsic factors are favorable for HEA 1000 alloy sample towards the reaction catalysis. The BET N_2 adsorption isotherm resembles a type 4 isotherm indicating a mesoporous nature, where a multilayer adsorbate formation occurs initially and then followed by the capillary condensation of the adsorbate inside the pores before reaching the saturation pressure of the adsorbate in the liquid form.[39] **Fig. S13b** shows the pore size distribution of the three HEACB samples, indicating that their pore size comes in the mesoporous range of 3 to 30 nm. These factors are favorable for the enhanced catalyst performance, as the high surface area offers more exposed active sites, improved electrolyte penetration, and faster ion diffusion through the heterojunction. This observation also thus justifies the C_{dl} measurement made for ECSA estimation as well as the observed activity trends. The better performance of the HEACB 1000 can be inferred as the high degree of formation of single-phase entropy alloy on the carbon matrix concerning the less temperature annealed HEACB 750 and HEACB 500, which is evident from the XRD analysis. Thus, the Cocktail effect of the five metals in the HEACB 1000 alloy, along with the extrinsic factors like surface area/ ECSA and better elemental distribution over the carbon, seems to reduce the energy barrier for these reactions by offering suitable and accessible active sites and optimizing the interaction with the reaction intermediates.

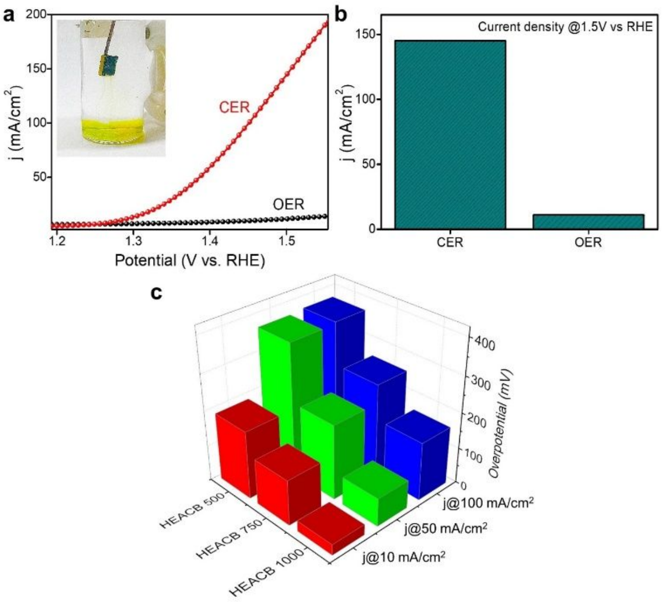

Fig. 6. (a) HEACB 1000 activity comparison in 0.5 M H2SO4 and 4 M NaCl reaction medium towards CER and OER and (b) the corresponding current density comparison plot at 1.5 V vs. RHE potential at the working electrode and (c) bar diagram showing the current carrying efficiency of HEACB 1000, 750 and 500 concerning their reaction overpotential.

One of the main hurdles in seawater hydrolysis is the oxidation of competing Cl^- and H_2O molecules so that thermodynamically more favorable OER would occur and hinders the CER process. Their selectivity and control are always of prime importance, especially when we plan for seawater electrolysis on a larger scale when such interfering ions can lead to unwanted reactions. **Fig. 6a** compares the CER and OER activity of the HEACB 1000 catalyst in two distinct electrolyte mediums. One medium comprises simulated seawater with a pH of 1 while the other has the same pH level but lacks chloride ions. Based on the LSV response, it is evident that at an acidic pH during the oxidation polarization region, the preferred reaction is CER while the competing reaction, OER, is significantly reduced. This demonstrates effective control over the selectivity of the two reactions. In a basic medium, we observed a significant increase in oxygen evolution during a similar reaction, while the rate of CER decreased. Thus, the catalyst HEACB 1000 was highly efficient in favoring the kinetics of these two competing reactions selectively based on the pH of the reaction media. **Fig. 6b** and **c** show the comparative abilities of the catalyst in driving current under a specific potential, which indirectly tells us about the exchange current density. The higher the exchange current density better the reaction kinetics, where HEACB 1000 came out to be the top-tier among the synthesized materials.

Mott Schottky (MS) analysis

The excellent catalytic activity of the high entropy metal alloy carbon composite and the need to disperse the high entropy alloy particle on a carbon frame can explain in terms of their metal-semiconductor heterojunctions formed at their interface. We utilize here the concept of Mott-Schottky analysis on our HEACB samples.[24] Since the alloy nanoparticle is dispersed onto conductive carbon support and the intimate interaction was inferred by Raman spectra **Fig. 1b**, we can expect to form a metal alloy/semiconductor interface. Electron flows are expected to occur during forming of such types of interfaces, where electron flows from an electron-dense system towards the lesser electron-dense side until the fermi level equilibrates.[51,52]

To investigate this phenomenon, we have performed a detailed Mott-Schottky analysis of HEACB 1000, HEACB 750, and HEACB 500, as indicated in **Fig. 7**, at a constant current frequency of 1 kHz and amplitude of 20 mV in the potential range of -0.2 to 1.2 V vs. RHE. The inverse capacitance square vs. the potential difference between the catalyst electrolyte

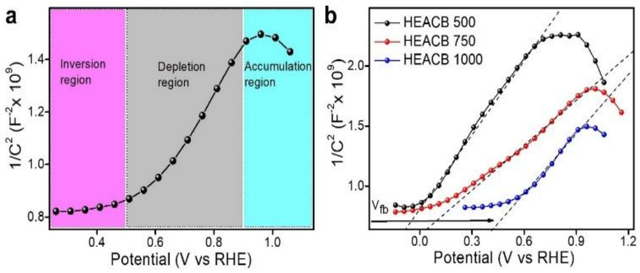

Fig. 7. (a) Mott-Schottky plots for HEACB 1000 showing different potential regions in an electrolytic solution of 1 M KOH. (b) Combined Mott-Schottky plots of HEACB 1000, 750, and 500 samples (X- intercept shows the respective flat band potential (V_{fb})).

interface verifies the existence of a metal-semiconductor junction in our system which is well evident by the formation of three distinct potential regions as shown in **Fig. 7a and b.** The positive slope of the plot indicates an n-type semiconductor behavior, where we expect the electron flow from the n-type carbon framework towards the alloy nanoparticles until their fermi level equilibrates, thus optimizing the HEA particles in terms of their band structure for efficient reaction catalysis.[24,53] We can extract two parameters from the graph: the flat band potential (V_{fb}) and charge carrier density. The X intercept of the MS plot (**Fig. 7b**) indicates the V_{fb} of each sample, and the magnitude of the slope refers to the charge carrier density.[54,55] If we compare the three HEACB samples, we could see a considerable shift in the flat band potential towards the positive side on going from HEACB 500 (-0.078 V) to HEACB 1000 (0.038V). This positive shift indicates that the Mott-Schottky junction formed is helping to reduce the band bending and thus favoring the faster charge transfer kinetics. This optimization was done at its best in the case of HEACB 1000 where the band bending is found to be the minimum. If we analyze the slope of the MS plot, we can see they are in the order HEACB 750<HEACB 1000<HEACB 500. Since the slope has an inverse relation with the charge carrier density, we can infer that the HEACB 750 and HEACB 1000 have comparatively much higher charge carrier densities than HEACB 500, which might be a factor that supports the relatively better activity in the catalysis of HER, OER, and CER. The parameters we extract from MS analysis always have direct implications for the kinetics of reactions. **Fig. 8a** and **S14** show the Tafel slope relationship with that of the flat band potential obtained from the MS analysis for HER, CER, and OER, respectively. We could see that for all three processes, the kinetics of the reaction and V_{fb} followed an exponential relation, where we spotted HEACB 1000 at the most optimized region of interaction for all these three processes, hence verifying our experimental observations. Thus, MS analysis gives us a clear picture of the relative band structure and carrier density on our synthesized alloy carbon composite and therefore supports the catalytic behavior of the samples.[51]

Total water splitting

The HEACB 1000 catalyst exhibits excellent HER and OER performance, suggesting the usage of this material as a catalyst in a practical water electrolyzer. To analyze the suitability of the catalyst in a real-life application, we have simulated the environment of an alkaline water electrolyzer setup with the bifunctional catalyst HEACB 1000 as both cathode and anode material.[56,57] 1 M KOH is used as the electrolyte medium, and LSVs are recorded at a scan rate of 10 mA/cm^2. As shown in **Fig. 8b,** we have tried the total water splitting with different combinations of anode and cathode materials, including the current state of art HER and OER catalysts, Pt/C, and RuO_2 respectively. From the plot, the HEACB 1000//HEACB 1000 system performed better with a potential of 1.65 V against RHE to reach a current density of 10 mA/cm^2 than RuO_2//RuO_2 and Pt/C//Pt/C systems towards total water splitting. The water-splitting performance of the HEACB 1000 couple is found to be close enough to that for RuO_2//Pt/C combinations. The overall performance of the HEACB 1000//HEACB 1000 system is better than many recently reported catalysts (**Table S10**). This suggests that the HEACB catalyst is a suitable candidate for total water splitting. To estimate how efficiently the catalyst utilizes the electrons to push the reaction of our interest, the estimation of faradaic efficiency (F.E) is quite important. The evolved gas was quantified during HER and OER reactions, and concomitant F.E. was deduced accordingly. The HEACB 1000 shows a decent level of F.E values with 87.3% and 91.5% for OER and HER, respectively. The exchange current density and turnover frequency (TOF) shed light on the intrinsic activity and the density of active sites existing in the catalyst material. HEACB 1000 shows a decent exchange current density of 7.5 cm^2, 14 cm^{2,} and 15.2 cm^2 for OER, HER, and CER, respectively, indicating the ability of the catalyst to promote efficient charge transfer. The TOF values derived from the active site density estimated from the non-faradic region of the catalyst in a neutral phosphate buffer show that the intrinsic activity of HEACB 1000 is comparatively better among the HEACB 750 and HEACB 500 (**Tables S6-S8, S11-S16, and Fig. S15**), which again justifies the high performance of HEACB 1000. In conclusion, the HEACB 1000 catalyst provides a reliable platform for complete seawater splitting with impressive catalytic parameters, such as TOF, exchange current density, and faradaic efficiency.

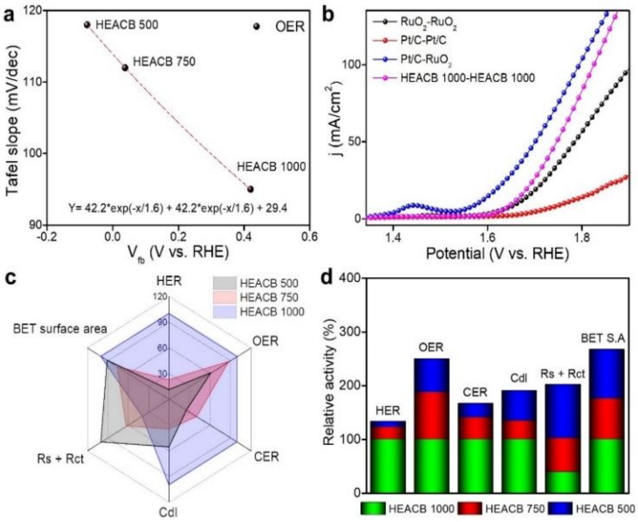

Fig. 8. (a) Tafel slope -flat band potential relationship plot for OER. (b) Total water splitting performance of HEACB samples in the OER polarization region in 1 M KOH. (c) Radar plot comparing with respect to their multifunctional behavior in terms of their relative activity percentages along with its respective bar diagram (d).

Since the catalyst is active for HER-CER in an acidic environment and HER-OER in a basic environment, this material can be used as a potential seawater electrolyzer with two modes of operation which are switchable concerning the pH of the electrolyte media, thus opening an avenue towards sustainable water splitting reaction for quality enhanced chemical productions. The radar and bar diagram in **Fig. 8c** and **d** show the multifunctional aspects of the three catalysts, along with their ECSA and impedance data comparison. The HEACB 1000 came upfront in the relative percentage activity which is visible from the illustrated radar plot (**Fig. 8c and S16-S17**). These figures strongly convey the multifunctional aspect of our synthesized HEA catalyst, thus emphasizing its ability to accelerate the kinetics using its multiple reaction sites instituted from the five different transition metals.

Conclusion

In summary, we have fabricated a novel conductive carbon-supported high entropy alloy (HEACB) based catalyst by employing a facile single-step pyrolysis technique at different synthetic temperatures to optimize the alloy particle formation. The HEACB 1000 sample shows great potential in electrocatalysis as it requires less overpotential and has lower onset and Tafel slopes for HER, OER, and CER reactions. It requires an overpotential of 190 mV, 350 mV, and 30 mV for HER, OER, and CER reactions to achieve a current density of 10 mA/cm^2. The enhanced catalytic performance of the HEACB 1000 concerning other synthesized samples is ascribed to the higher degree of alloy formation, incorporated multi-metallic active site, and intimate contact with carbon catalytic bed, thus inducing a synergistic effect and optimizing the interaction with intermediates formed during the reaction. The catalyst performs well in selectively producing CER and OER reactions, depending on the pH of the reaction media. It exhibits good stability and durability in the complete water-splitting process, with a half-cell potential of 1.65 V. The catalyst's band structure and charge transfer efficiency were analyzed through Mott-Schottky analysis, impedance spectroscopy, and other structural characterizations. This works points to a novel strategy to design and synthesize high entropy alloy-based catalyst through a simple feasible technique with a detailed study of the possible interaction at the heterojunction. This strategy can be applied to other transition metals, resulting in a cost-effective and dependable catalyst for complete seawater splitting.

Experimental section

Materials and reagents

Chromium (III) nitrate hexahydrate ($Cr(NO_3)_3.6H_2O$, M.W= 346.10 g/mol), Manganese(II)nitrate hexahydrate ($Mn(NO_3)_2{\cdot}6H_2O$, M.W= 287.04 g/mol) Iron(III) nitrate hexahydrate ($Fe(NO_3)_3.6H_2O$, M.W= 349.9 g/mol), Cobalt(II) nitrate hexahydrate ($Co(NO_3)_2{\cdot}6H_2O$, M.W= 291.03 g/mol), Nickel(II) nitrate hexahydrate ($Ni(NO_3)_2{\cdot}6H_2O$, M.W= 290.79 g/mol), and carbon black (CAS number: 1333-86-4 required for the synthesis were purchased from Sigma-Aldrich and used as received. Potassium hydroxide (KOH, M. W= 56.11 g/mol) pellets, sulphuric acid (H_2SO_4, 99.9%, M. W= 98.08 g/mol), sodium chloride (NaCl, M. W= 58.44 g/mol), hydrochloric acid (36%, M. W= 36.46 g/mol) from the same manufacturer were used for electrochemical studies.

Synthesis of Materials

The equimolar (0.5M) aqueous solution of Chromium (III) nitrate hexahydrate ($Cr(NO_3)_3.6H_2O$, M.W= 346.10 g/mol), Manganese (II) nitrate hexahydrate ($Mn(NO_3)_2{\cdot}6H_2O$, M.W= 287.04 g/mol) Iron (III) nitrate hexahydrate ($Fe(NO_3)_3.6H_2O$, M.W= 349.9 g/mol), Cobalt (II) nitrate hexahydrate ($Co(NO_3)_2{\cdot}6H_2O$, M.W= 291.03 g/mol), Nickel (II) nitrate hexahydrate ($Ni(NO_3)_2{\cdot}6H_2O$, M.W= 290.79 g/mol) were brewed up separately and assorted gently under constant and continuous stirring by employing a magnetic stirrer, calorified to a small temperature of about 50 ^{o}C to enhance the precursor miscibility. After two hours of continuous temperature treatment on a magnetic hot plate, about 2 g of carbon black and 15 mL of ethanol were blended with the above-procured solution. This mixture was stirred at 200 rpm, maintaining the same temperature to ensure homogeneous mixing of metal cations to ensure high reaction probability. The above heat treatment was followed by freeze drying to yield a fluffy darkish brown precursor powder. Using a mortar pestle, this powder was ground well and then subjected to high-temperature pyrolysis of about 1000 ^{o}C with an effective ramping rate of 10 ^{o}C/ min and dwelling time of about two hours in an inert protected environment on a tube furnace setup under a constant Nitrogen gas flow of about 100 sccm. For optimizing the synthesis strategy and to have a comparative study of samples having different degrees of HEA alloy incorporation, three independent samples were fabricated at different synthesis temperatures of 500, 750, and 1000 ^{o}C, which were then labeled as HEACB 500, HEACB 750, and HEACB 1000 respectively for further analysis.

Characterizations

In the preliminary phase of the investigation, we subjected the samples for crystal structural assessment using X-ray diffraction studies (XRD) by employing an X-ray diffractometer (PANalytical) with a monochromatized Cu $K\alpha$ radiation of 1.54 Å wavelength. Direct visualization of the morphology of the sample was obtained by utilizing a scanning electron microscope (SEM) FESEM FEI inspect 50 and transmission electron microscope (TEM) Tecnai T20 microscope with an accelerating voltage of 200 kV. X-ray photoelectron spectrometer AXIS ULTRA DLD Kratos possessing a monochromatic Al $K\alpha$ radiation source of 1486.6 eV, was used to render high-resolution X-ray photoelectron spectroscopy (HR-XPS) of individual elements, to examine the elemental composition, oxidation states, and the various chemical bonds existing in the catalytic material.

Electrochemical measurements

The electrochemical studies were accomplished using a CHI 750E based Instrument supporting a three-electrode configuration, where a commercial glassy carbon electrode (GCE) of 0.07 cm^2 and rotating ring disk electrode (RRDE) of 0.196 cm^2 geometrical surface area were employed as the major reaction working electrodes, Ag/AgCl electrode taken as the reference electrode, and platinum wire used as the counter electrode. The GCE and RRDE were well polished with alumina powder of an average particle size of 0.005 µm to procure an atomically smooth electrode surface. About 7 mg of catalyst material is added to 1000 µL ethanol-water mixture followed by 20 µL of 5 wt% Nafion 117 solution and is then sonicated for 15 min to obtain a well-dispersed thick catalyst ink. 7 µL of this catalyst ink was used for each electrochemical study. IR compensation is done during each measurement to minimize the uncompensated solution resistance. All LSV measurements were taken at a scan rate of 5 mV sec^{-1} with RDE unless specified separately.

AUTHOR INFORMATION

Corresponding Authors

Jongbeom Na: ORCID 0000-0002-3890-7877
E-mail: jongbeom@kist.re.kr

Karuna Kar Nanda: ORCID 0000-0001-9496-1408
E-mail: nanda@iisc.ac.in

Author Contributions

G. R.: performed a majority of experiments, materials synthesis, methodology, conceptualization, structural and electrochemical data curation, analysis, writing, and editing of the manuscript. R. N: Material synthesis, methodology, conceptualization, scientific discussion, review, and editing of the manuscript. K. K.: XPS data acquisition and analysis, SEM imaging, BET, Raman spectroscopy, writing manuscript, and its editing. D. B. G.: CER conceptualization and its electrochemical measurements, manuscript writing, and its editing. A. B. M: TEM imaging, J.N.: Image processing, manuscript review-editing-writing. J.K.: manuscript review-writing. Y.Y.: Scientific discussion, conceptualization, experimental suggestions, review, and editing of the manuscript. K. K. N Conceptualization, funding acquisition, supervision, scientific discussion, project administration, review, and editing of the manuscript. All the authors agreed to the final version of the manuscript.

Funding Sources

Ministry of Human Resource Development (MHRD)
Department of Science and Technology (DST), India
Japan Society for the Promotion of Science (JSPS)

Notes

[#] Authors have equally contributed.

Conflicts of interest

There are no conflicts to declare.

ACKNOWLEDGMENT

G.R. would like to thank the Ministry of Human Resource Development (MHRD) for the research scholarship. The authors also acknowledge the Department of Science and Technology (DST), India, for funding the BET adsorption-desorption facility (DST-SERB, EMR/2016/005843 and DST-FIST, SR/FST/PSII-009/2010) for the research. R.N. and Y.Y. acknowledge financial support from the Japan Society for the Promotion of Science (JSPS, No. P22063), the UQ-Yonsei Univ. International Project, the JST-ERATO Yamauchi Materials Space-Tectonics Project (JPMJER2003), and J.N. acknowledges financial support from the KIST institutional program (2E32511). This work has been supported by the Researchers Supporting Project (RSP2023R405) from King Saud University. The authors would like to acknowledge the Materials Research Centre (MRC) for providing the XRD facility, the Centre for Nanoscience and Engineering (CeNSE), IISc for providing the SEM facility, and the Advanced Facility for Microscopy and Microanalysis (AFMM) for the TEM facility. Additionally, the authors are grateful to Dr. Omeshwari Bisen and Dr. Hemam Rachana Devi in the Materials Research Centre, IISc Bangalore, for their help with BET analysis, Raman spectroscopic measurements, and helpful scientific discussions. This work was performed in part at the Queensland node of the Australian National Fabrication Facility, a company established under the National Collaborative Research Infrastructure Strategy to provide nano and microfabrication facilities for Australia's researchers.

Appendix

Equations used for the calculation of Faradaic Efficiency (F.E)[58]

$$F.E = Q_{experimental} / Q_{Theoretical} = VnF/(V_m A)$$

V = Volume of gas evolved in liters
V_m = Molar Volume of gas at 298K (24.5L)
n = Number of electrons involved
F = Faradaic constant (96485 C)
A = Integral area of current response with time

Equations used for the calculation of exchange current density

$$J_0 = RT/(nFR_{ct})$$

J_o = exchange current density
R = Gas constant 8.314 J/K
n = No. of electrons involved
F = Faradaic constant (96485 C)

R_{ct} = Charge transfer resistance
A = Area of electrode

Equations used for the calculation of Turn Over Frequency (TOF)

$TOF = |J| \times A / (n \times F \times N)$

$N = S / (2 \times F \times u)$
J = Current density
A = Area of electrode
n = No. of electrons involved in the reaction
F = Faradaic constant
N = Active site density
S = Integral area of cyclic voltammetry response in the non-faradaic region in a neutral pH phosphate buffer
u = Scan rate (V/sec)

References

1 D. B. Miracle and O. N. Senkov, *Acta Mater.*, 2017, **122**, 448–511.
2 D. Sauceda, P. Singh, G. Ouyang, O. Palasyuk, M. J. Kramer and R. Arróyave, *Mater. Horizons*, 2022, **9**, 2644–2663.
3 V. Chaudhary, R. Chaudhary, R. Banerjee and R. V Ramanujan, *Mater. Today*, 2021, **49**, 231–252.
4 S. Akrami, P. Edalati, M. Fuji and K. Edalati, *Mater. Sci. Eng. R Reports*, 2021, **146**, 100644.
5 M. W. Glasscott, *Curr. Opin. Electrochem.*, 2022, **34**, 100976.
6 Y. Wang, Y. Wu, K. Sun and Z. Mi, *Mater. Horizons*, 2019, **6**, 1454–1462.
7 S. S. Jana and T. Maiti, *Mater. Horiz.*, 2023.
8 Y. Kang, B. Jiang, J. Yang, Z. Wan, J. Na, Q. Li, H. Li, J. Henzie, Y. Sakka, Y. Yamauchi and T. Asahi, *ACS Nano*, 2020, **14**, 17224–17232.
9 P. Li, Y. Yao, W. Ouyang, Z. Liu, H. Yin and D. Wang, *J. Mater. Sci. Technol.*, , DOI:https://doi.org/10.1016/j.jmst.2022.08.012.
10 A. K. Ipadeola, A. K. Lebechi, L. Gaolatlhe, A. B. Haruna, M. Chitt, K. Eid, A. M. Abdullah and K. I. Ozoemena, *Electrochem. Commun.*, 2022, **136**, 107207.
11 Q. Zeng and Y. Xu, *Mater. Today Commun.*, 2020, **24**, 101261.
12 Y. Shi, B. Yang and P. K. Liaw, *Metals (Basel).*, DOI:10.3390/met7020043.
13 H. Lv, D. Xu, L. Sun, J. Henzie, S. L. Suib, Y. Yamauchi and B. Liu, *ACS Nano*, 2019, **13**, 12052–12061.
14 M. A. Aktar, M. M. Alam and A. Q. Al-Amin, *Sustain. Prod. Consum.*, 2021, **26**, 770–781.
15 A. Kumar, P. Singh, P. Raizada and C. M. Hussain, *Sci. Total Environ.*, 2022, **806**, 150349.
16 I. Mauleón, *Energies*, , DOI:10.3390/en14154657.
17 M. Mohsin, H. W. Kamran, M. Atif Nawaz, M. Sajjad Hussain and A. S. Dahri, *J. Environ. Manage.*, 2021, **284**, 111999.
18 R. R. Salunkhe, J. Tang, Y. Kamachi, T. Nakato, J. H. Kim and Y. Yamauchi, *ACS Nano*, 2015, **9**, 6288–6296; R. Nandan, G. K. Goswami, and K. K. Nanda, *Appl Energy*, 2017, **205**, 1050–1058; R. Nandan, N. Takamori, K. Higashimine, R. Badam and N. Matsumi, *J Mater Chem A Mater*, 2022, **10**, 15960–15974; R. Nandan, N. Takamori, K. Higashimine, R. Badam and N. Matsumi, *J Mater Chem A Mater*, 2022, **10**, 5230–5243; R. Nandan, O. Y. Bisen and K. K. Nanda, *Journal of Physical Chemistry C*, 2021, **125**, 10378–10385.
19 Z.-X. Cai, Y. Xia, Y. Ito, M. Ohtani, H. Sakamoto, A. Ito, Y. Bai, Z.-L. Wang, Y. Yamauchi and T. Fujita, *ACS Nano*, 2022, **16**, 20851–20864.
20 J. Qi, W. Zhang and R. Cao, *Adv. Energy Mater.*, 2018, **8**, 1701620.
21 X. Yang, R. Guo, R. Cai, Y. Ouyang, P. Yang and J. Xiao, *Int. J. Hydrogen Energy*, 2022, **47**, 13561–13578.
22 C.-L. Huang, K. Sasaki, D. Senthil Raja, C.-T. Hsieh, Y.-J. Wu, J.-T. Su, C.-C. Cheng, P.-Y. Cheng, S.-H. Lin, Y. Choi, and S.-Y. Lu, *Adv. Energy Mater.*, 2021, **11**, 2101827.
23 A. A. Koverga, E. Flórez and J. A. Rodriguez, *Int. J. Hydrogen Energy*, 2021, **46**, 25092–25102.
24 G. Raj, D. Das, B. Sarkar, S. Biswas and K. K. Nanda, *Sustain. Mater. Technol.*, 2022, **33**, e00451.
25 R. Nandan, G. Raj and K. K. Nanda, *ACS Appl. Mater. Interfaces*, 2022, **14**, 16108–16116; R. Nandan, M. Y. Rekha, H. R. Devi, C. Srivastava and K. K. Nanda, *Chemical Communications*, 2021, **57**, 611–614
26 J. Liu, C. Tang, Z. Ke, R. Chen, H. Wang, W. Li, C. Jiang, D. He, G. Wang and X. Xiao, *Adv. Energy Mater.*, 2022, **12**, 2103301.
27 H. Li, Y. Han, H. Zhao, W. Qi, D. Zhang, Y. Yu, W. Cai, S. Li, J. Lai, B. Huang and L. Wang, *Nat. Commun.*, 2020, **11**, 5437.
28 S. Wu, Y. Pan, N. Wang, T. Lu and W. Dai, *Int. J. Miner. Metall. Mater.*, 2019, **26**, 124–132.
29 J. K. Pedersen, T. A. A. Batchelor, A. Bagger and J. Rossmeisl, *ACS Catal.*, 2020, **10**, 2169–2176.
30 S. Nellaiappan, N. K. Katiyar, R. Kumar, A. Parui, K. D. Malviya, K. G. Pradeep, A. K. Singh, S. Sharma, C. S. Tiwary and K. Biswas, *ACS Catal.*, 2020, **10**, 3658–3663.
31 V. Márquez, M. Fereidooni, J. S. Santos, S. Praserthdam and P. Praserthdam, *Electrochim. Acta*, , DOI:10.1016/j.electacta.2022.140975.
32 L. Fan, Y. Ji, G. Wang, J. Chen, K. Chen, X. Liu and Z. Wen, *J. Am. Chem. Soc.*, 2022, **144**, 7224–7235.
33 Y. Liu, K. Wang, X. Xu, K. Eid, A. M. Abdullah, L. Pan and Y. Yamauchi, *ACS Nano*, 2021, **15**, 13924–13942.
34 J. Huang, M. Hou, J. Wang, X. Teng, Y. Niu, M. Xu and Z. Chen, *Electrochim. Acta*, 2020, **339**, 135878.
35 Y. Gendel, G. Amikam and P. Nativ, eds. T. Smolinka and J. B. T.-E. P. S. F. Garche Systems, and Applications, Elsevier, 2022, pp. 305–326.
36 H. Li, J. Lai, Z. Li and L. Wang, *Adv. Funct. Mater.*, 2021, **31**, 2106715.
37 Y. Wang, Y. Nian, A. N. Biswas, W. Li, Y. Han and J. G. Chen, *Adv. Energy Mater.*, 2021, **11**, 2002967.
38 Y. Tang, C. Yang, X. Xu, Y. Kang, J. Henzie, W. Que and Y. Yamauchi, *Adv. Energy Mater.*, 2022, **12**, 2103867.

39 Y. Yin, J. Wang, T. Li, J. P. Hill, A. Rowan, Y. Sugahara and Y. Yamauchi, *ACS Nano*, 2021, **15**, 13240–13248.

40 H. R. Devi, R. Nandan and K. K. Nanda, *ACS Appl. Mater. Interfaces*, 2020, **12**, 13888–13895.

41 Y. Peng and S. Chen, *Green Energy Environ.*, 2018, **3**, 335–351; R. Nandan, P. Pandey, A. Gautam, O. Y. Bisen, K. Chattopadhyay, M. M. Titirici and K. K. Nanda, *ACS Appl Mater Interfaces*, 2021, **13**, 3771–3781; R. Nandan, A. Gautam and K. K. Nanda, *J Mater Chem A Mater*, 2018, **6**, 20411–20420.

42 M. N. Kirikova, A. S. Ivanov, S. V Savilov and V. V Lunin, *Russ. Chem. Bull.*, 2008, **57**, 298–303.

43 C. V. M. Inocêncio, Y. Holade, C. Morais, K. B. Kokoh and T. W. Napporn, *Electrochem. Sci. Adv.*, 2022, **n/a**, e2100206.

44 S. Shiva Kumar and V. Himabindu, *Mater. Sci. Energy Technol.*, 2019, **2**, 442–454.

45 H. Jing, P. Zhu, X. Zheng, Z. Zhang, D. Wang and Y. Li, *Adv. Powder Mater.*, 2022, **1**, 100013.

46 N. L. W. Septiani, Y. V. Kaneti, K. B. Fathoni, Y. Guo, Y. Ide, B. Yuliarto, X. Jiang, , Nugraha, H. K. Dipojono, D. Golberg and Y. Yamauchi, *J. Mater. Chem. A*, 2020, **8**, 3035–3047.

47 M. Liu, B. Niu, H. Guo, S. Ying and Z. Chen, *Inorg. Chem. Commun.*, 2021, **130**, 108687; R. Nandan, A. Gautam, S. Tripathi and K. K. Nanda, *J Mater Chem A Mater*, 2018, **6**, 8537–8548; R. Nandan, A. Gautam and K. K. Nanda, *J Mater Chem A Mater*, 2017, **5**, 20252–20262.

48 Y. Yan, J. Lin, T. Xu, B. Liu, K. Huang, L. Qiao, S. Liu, J. Cao, S. C. Jun, Y. Yamauchi and J. Qi, *Adv. Energy Mater.*, 2022, **12**, 2200434.

49 T. Chouki, B. Donkova, B. Aktarla, P. Stefanov and S. Emin, *Mater. Today Commun.*, 2021, **26**, 101976.

50 M. Natalia, Y. N. Sudhakar and M. Selvakumar, *Indian J. Chem. Technol.*, 2013, **20**, 392–399.

51 X. Ji, K. Wang, Y. Zhang, H. Sun, Y. Zhang, T. Ma, Z. Ma, P. Hu, and Y. Qiu, *Sustain. Energy Fuels*, 2020, **4**, 407–416.

52 B. Sarkar, D. Das and K. K. Nanda, *J. Mater. Chem. A*, 2021, **9**, 13958–13966.

53 Z.-H. Xue, H. Su, Q.-Y. Yu, B. Zhang, H.-H. Wang, X.-H. Li and J.-S. Chen, *Adv. Energy Mater.*, 2017, **7**, 1602355.

54 J. Hou, Y. Sun, Y. Wu, S. Cao and L. Sun, *Adv. Funct. Mater.*, 2018, **28**, 1704447.

55 H. Zhong, C. Yang, L. Fan, Z. Fu, X. Yang, X. Wang and R. Wang, *Energy Environ. Sci.*, 2019, **12**, 418–426.

56 Y. Xu, J. Yang, T. Liao, R. Ge, Y. Liu, J. Zhang, Y. Li, M. Zhu, S. Li and W. Li, *Chem. Eng. J.*, 2022, **431**, 134126.

57 W. Luo, Y. Wang, L. Luo, S. Gong, Y. Li and X. Gan, *Appl. Surf. Sci.*, 2022, **606**, 154808.

58 T. ul Haq, S. A. Mansour, A. Munir, and Y. Haik, *Adv. Funct. Mater.*, 2020, **30**, 1910309; J. Tong, Y. Li, L. Bo, W. Li, T. Li, Q. Zhang, D. Kong, H. Wang and C. Li, *ACS Sustain. Chem. Eng.*, 2019, **7**, 17432–17442.